

v1 November 6, 2018

## On the nature of the first galaxies selected at $350\ \mu\text{m}$

Sophia A. Khan<sup>1,2,3,4,5</sup>, Pierre F. Chanial<sup>2</sup>, S. P. Willner<sup>4</sup>, Chris P. Pearson<sup>6,7</sup>, M. L. N. Ashby<sup>4</sup>, Dominic J. Benford<sup>3</sup>, David L. Clements<sup>2</sup>, Simon Dye<sup>8</sup>, Duncan Farrah<sup>9,10</sup>, G. G. Fazio<sup>4</sup>, J.-S. Huang<sup>4</sup>, V. Leboutteiller<sup>10</sup>, Emeric Le Floc'h<sup>11</sup>, Gabriele Mainetti<sup>12</sup>, S. Harvey Moseley<sup>3</sup>, Mattia Negrello<sup>13</sup>, Stephen Serjeant<sup>13</sup>, Richard A. Shafer<sup>3</sup>, Johannes Staguhn<sup>3,14</sup>, Timothy J. Sumner<sup>2</sup>

and

Mattia Vaccari<sup>15</sup>

### ABSTRACT

We present constraints on the nature of the first galaxies selected at  $350\ \mu\text{m}$ . The sample includes galaxies discovered in the deepest blank-field survey at

---

<sup>1</sup>ALMA Fellow, Pontificia Universidad Católica, Departamento Astronomía y Astrofísica, 4860 Vicuña Mackenna, Casilla 406, Santiago 22 Chile

<sup>2</sup>Imperial College London, Blackett Laboratory, Prince Consort Road, London SW7 2AZ, UK

<sup>3</sup>Observational Cosmology Laboratory (Code 665), NASA Goddard Space Flight Center, Greenbelt, MD 20771 USA

<sup>4</sup>Harvard-Smithsonian Center for Astrophysics, 60 Garden Street, Cambridge, MA 02138 USA

<sup>5</sup>Shanghai Key Lab for Astrophysics, Shanghai Normal University, Shanghai 200234, China

<sup>6</sup>Rutherford Appleton Laboratory, Chilton, Didcot, Oxfordshire OX11 0QX, UK

<sup>7</sup>Department of Physics, University of Lethbridge, 4401 University Drive, Lethbridge, Alberta T1J 1B1, Canada

<sup>8</sup>School of Physics and Astronomy, Cardiff University, Queens Buildings, Cardiff, CF24 3AA, UK

<sup>9</sup>Astronomy Centre, University of Sussex, Falmer, Brighton UK

<sup>10</sup>Department of Astronomy, Cornell University, 610 Space Sciences Building, Ithaca, NY 14853 USA

<sup>11</sup>*Spitzer* Fellow, Institute for Astronomy, University of Hawaii, 2680 Woodlawn Drive, Honolulu, HI 96815 USA

<sup>13</sup>Department of Physics and Astronomy, Open University, Walton Hall, Milton Keynes MK7 6AA, UK

<sup>14</sup>Department of Astronomy, University of Maryland, College Park, MD 20742 USA

<sup>15</sup>Department of Astronomy, University of Padova, Vicolo Osservatorio 3, I-35122, Padova, Italy

350  $\mu\text{m}$  (in the Boötes Deep Field) and also later serendipitous detections in the Lockman Hole. In determining multiwavelength identifications, the 350  $\mu\text{m}$  position and map resolution of the second generation Submillimeter High Angular Resolution Camera (SHARC II) are critical, especially in the cases where multiple radio sources exist and the 24  $\mu\text{m}$  counterparts are unresolved. Spectral energy distribution templates are fit to identified counterparts, and the sample is found to comprise IR-luminous galaxies at  $1 < z < 3$  predominantly powered by star formation. The first spectrum of a 350  $\mu\text{m}$ -selected galaxy provides an additional confirmation, showing prominent dust grain features typically associated with star-forming galaxies.

Compared to submillimeter galaxies selected at 850 and 1100  $\mu\text{m}$ , galaxies selected at 350  $\mu\text{m}$  have a similar range of far-infrared color temperatures. However, no 350  $\mu\text{m}$ -selected sources are reliably detected at 850 or 1100  $\mu\text{m}$ . Galaxies in our sample with redshifts  $1 < z < 2$  show a tight correlation between the far- and mid-infrared flux densities, but galaxies at higher redshifts show a large dispersion in their mid- to far-infrared colors. This implies a limit to which the mid-IR emission traces the far-IR emission in star-forming galaxies.

The 350  $\mu\text{m}$  flux densities ( $15 < S_{350} < 40$  mJy) place these objects near the *Herschel*/SPIRE 350  $\mu\text{m}$  confusion threshold, with the lower limit on the star formation rate density suggesting the bulk of the 350  $\mu\text{m}$  contribution will come from less luminous infrared sources and normal galaxies. Therefore the nature of the dominant source of the 350  $\mu\text{m}$  background — star-forming galaxies in the epoch of peak star formation in the universe — could be more effectively probed using ground-based instruments with their angular resolution and sensitivity offering significant advantages over space-based imaging.

*Subject headings:* infrared: galaxies – submillimeter: galaxies – galaxies: starburst – galaxies: high-redshift

## 1. Introduction

Submillimeter-selected galaxies (SMGs) were discovered in pioneering lensed and blank-field surveys (e.g., Smail, Ivison & Blain 1997; Barger et al. 1998; Eales et al. 1999) with the 850  $\mu\text{m}$ -optimised Submillimeter Common User Bolometer Array (SCUBA; Holland et al. 1999) and later in similar surveys with millimeter detectors (e.g., MAMBO, BOLOCAM, etc.: Bertoldi et al. 2000; Laurent et al. 2005). SMGs mainly comprise massive, star-forming galaxies (see, e.g., Fox et al. 2002) around  $z \sim 2$  (Chapman et al. 2005) with the bulk of

the emission generated at rest-frame far-IR wavelengths. SMGs are thus part of the IR-luminous galaxy population, which includes galaxies found in the local universe by the Infrared Astronomical Satellite (*IRAS*) All Sky Survey (Soifer et al. 1984; Joseph & Wright 1985; Soifer et al. 1987) and other galaxies detected in mid- and far-IR bands, most notably (in terms of number selected) with the *Infrared Space Observatory* (Kessler et al. 1996), the *Spitzer Space Telescope* (Werner et al. 2004) and the *Akari Infrared Satellite* (Murakami et al. 2007) out to  $z \sim 2$  (see, e.g., Rowan-Robinson et al. 1997; Puget et al. 1999; Aussel, Elbaz, & Cesarsky 1999; Elbaz et al. 2002; Chary et al. 2004; Lonsdale et al. 2004; Le Floc’h et al. 2004; Yan et al. 2004; Le Floc’h et al. 2005; Matsuhara 2006).

The majority of SMGs have been selected at long submillimeter–millimeter bands (500–1300  $\mu\text{m}$ ). Shorter submillimeter wavelengths (200–500  $\mu\text{m}$ ) are more demanding for ground-based observers. For example, on a good night at Mauna Kea, atmospheric transmission is about  $\sim 30\%$  at 350  $\mu\text{m}$  but  $\gtrsim 80\%$  at 850  $\mu\text{m}$ ; (Serabyn et al. 1998). Despite this, the first galaxy selected *purely* by 350  $\mu\text{m}$  emission — SMM J143206.65+341613.4 (=SSG 1, Short Submillimeter Galaxy 1) — was discovered (Khan et al. 2005) in a deep, blank survey of the Boötes Deep Field with the second generation Submillimeter High Angular Resolution Camera (SHARC II; Dowell et al. 2003; Moseley et al. 2004) along with a second detection, SMM J143206.11+341648.4 (=SSG 2; Khan 2006; Khan et al. 2007). This survey, reaching 13 mJy and currently the deepest at 350  $\mu\text{m}$ , obtained the first constraints on the 350  $\mu\text{m}$  source counts. Three additional 350  $\mu\text{m}$ -selected galaxies have been found in serendipitous SHARC II follow-up observations of 850  $\mu\text{m}$  and 1100  $\mu\text{m}$  SMGs in the Lockman Hole (Laurent et al. 2006; Coppin et al. 2008).

Short-wavelength submillimeter surveys are expected to principally select star-forming galaxies at  $1 < z < 3$  (see, e.g., Pearson & Khan 2009; Khan et al. 2007; Khan 2006), the epoch of peak star formation in the universe (e.g., Hopkins & Beacom 2006). Source count models that reproduce the observed 350  $\mu\text{m}$  counts include a predominantly IR-luminous galaxy population evolving with redshift (e.g., Pearson & Khan 2009; Franceschini et al. 2009), but more observations are needed to verify these predictions.

This paper presents a detailed characterization of each of the five 350  $\mu\text{m}$ -selected galaxies following the approach of Khan et al. (2005). Multiwavelength data are presented, and spectral energy distribution (SED) template fitting is used to provide constraints on the photometric redshifts, thermal parameters (IR luminosity and dust temperature), and energy diagnostics. Additionally the first mid-IR spectrum of a 350  $\mu\text{m}$ -selected galaxy, obtained using *Spitzer’s* Infrared Spectrograph (Houck et al. 2004), is given. The properties of the sample are compared with 850 and 1100  $\mu\text{m}$ -selected SMGs. Table 1 identifies the five sources and includes short nicknames used for convenience. The *WMAP* first year cosmolog-

ical parameters ( $H_0 = 71 \text{ km s}^{-1} \text{ Mpc}^{-1}$ ,  $\Omega_m=0.27$ ,  $\Omega_\Lambda=0.73$ ; Bennett et al. 2003) are used throughout this work.

## 2. Observations, data reduction, and counterpart identification

### 2.1. Observations

The SHARC II observations, data reduction, and source extraction procedure for the Boötes Deep Field survey are discussed in detail by Khan et al. (2007). Further details of source extraction are given by Khan (2006). Monte Carlo simulations for determining the survey completeness also provide a measure of the flux boosting. Approximately 4000 artificial sources of random intensity and position were inserted into the raw data map, then extracted using the same procedure as for the real sources (Khan et al. 2007). For recovered  $\geq 3\sigma$  sources with input flux densities  $>15 \text{ mJy}$ , the ratio of measured flux density to input flux density indicates the average flux boosting is  $1.07 \pm 0.23$ . Given the multiwavelength confirmation on SSG 1 and SSG 2, low outliers can be ruled out. Therefore we proceed without applying a correction factor to these sources and assume this also holds for the sources in the Lockman Hole. For the Lockman Hole, published  $350 \mu\text{m}$  flux densities were combined with public  $B$ ,  $R$ ,  $I$ , and  $z$  photometry from the Subaru Lockman Hole survey (Dye et al. 2008),  $K$  band imaging from UKIDSS (Lawrence et al. 2007), archival *Spitzer* IRAC and MIPS imaging, and 1.4 GHz data from Biggs & Ivison (2006). These compiled photometric data are presented in Table 2.

Additional 1.2 mm photometry of SSG 1 was obtained using MAMBO in 2005 January for  $\sim 3$  hours in photometry mode. The horn antenna design produces incomplete sampling of the field, and because there was no jiggling, SSG 2 was not observed. The data were reduced using the standard package (MOPSIC).

New VLA observations of the Boötes Deep Field were obtained on 2006 April 11. The VLA was in A configuration, giving a synthesized beam size of  $1''.36 \times 1''.50$  at 1.5 GHz. Wide field imaging mode was used in order to avoid bandwidth smearing: two 25 MHz IFs of two polarizations each with 7 channels per IF. The phase center was located  $10''$  north of SSG 1 to avoid any possible phase center artifacts. Standard wide field imaging techniques were employed, including self-calibration and 3D corrections. The final image was generated with AIPS parameter ROBUST = 1, giving an rms noise  $\approx 10 \mu\text{Jy}/\text{beam}$ . Automatic source search and flux density measurements were done with AIPS task SAD. Both SSG 1 and 2 were detected, but neither was spatially resolved.

Initial *Spitzer*/IRAC (Fazio et al. 2004) and MIPS (Rieke et al. 2004) data were ob-

tained during surveys of the NOAO Deep Wide Field in Boötes (Eisenhardt et al. 2004). Significantly deeper observations were later obtained in 2006 February as part of the IRAC GTO program (Program ID 520). The IRAC observations consisted of six dithered 100 s frames in each IRAC field of view, covering the SHARC II survey area in all four IRAC bands. Multiplexer bleed and other detector artifacts were removed by applying the *Spitzer* Science Center’s artifact mitigation code to the S14 version of the automated IRAC pipeline Basic Calibrated Data products. These cosmetically enhanced frames were then mosaiced using IRACProc v4.0beta (Schuster, Marengo & Patten 2006) to ensure correct treatment of the noise for both point and extended sources. The MIPS observations consisted of eight 30 s cycles at  $24\ \mu\text{m}$  only and covered the entire  $350\ \mu\text{m}$  map area. The data were reduced following standard procedures (Gordon et al. 2005), and source flux densities were measured with PSF fitting. The 99% confidence region of SSG 1 contains two visible-wavelength sources. The new  $24\ \mu\text{m}$  imaging shows that the source chosen as the most likely submm counterpart by Khan et al. (2005) is responsible for  $\sim 75\%$  of the  $24\ \mu\text{m}$  emission.

The *Spitzer*/IRS observation of SSG 1 was designed according to the recommended SSC set-up. For each slit, there were six pointings along the slit at  $24''$  spacing, all centered on the slit in its narrow dimension. This is equivalent to the normal point source method except that the target is observed in six different slit positions instead of the usual two, lessening the effects of flat-fielding errors and bad pixels. In 3.1 hours (the total for the AOR, including peakups and overheads), there were five cycles of LL1 ( $19.5\text{--}38.0\ \mu\text{m}$ ) and seven of LL2 ( $14.0\text{--}21.3\ \mu\text{m}$ ) with 120 s ramps at each of the six slit positions. The data were reduced using the pipeline S15, cleaned using IRSCLEAN, and extracted with SMART (Higdon et al. 2004). Two extraction techniques were compared: the first method involved extracting the spectra from the individual images and taking the median spectrum; the second method was to align the images, and then extract the spectrum. There was little difference in the final spectrum using either technique, and the spectrum is shown in Figure 1. The most prominent features in the SSG 1 spectrum are due to polycyclic aromatic hydrocarbons (PAH). For quantitative analysis, PAH can be measured from integrating the flux above a baseline, but this method tends to underestimate the flux density as compared to a profile decomposition method such as the one used by PAHFIT (Smith et al. 2007; see also Galliano et al. 2008 for more detailed consideration of the two approaches). While both methods give similar PAH ratios and similar spatial variations of PAH strengths, absolute flux densities will differ due to assumptions about the PAH profiles.

## 2.2. Counterpart Identification

The additional deep  $24\ \mu\text{m}$  and 1.4 GHz imaging of the Boötes field yielded counterparts in these bands for SSG 1 and 2 with low probabilities of chance association (Khan et al. 2007). The more precise positions were then used to identify optical and mid-IR counterparts. Finding counterparts for the three sources in the Lockman Hole is not straightforward: Figure 2 shows thumbnail images of the fields at various wavelengths. As can be seen, there exist multiple radio detections for two of the  $350\ \mu\text{m}$  objects. However the *most likely* counterparts can be determined with the following rationale:

- LH 350.1: the 1.4 GHz image shows two potential counterparts, but only the southern one is within the  $9''$  SHARC II beam. In the visible images this appears to be a blend of two sources. The photometric redshift for this southerly source was obtained using HYPER-Z (Bolzonella, Miralles & Pell’o 2000) in conjunction with the *BRIzJK*[3.6][4.5] photometry, similar to the approach of Dye et al. (2008). The best-fitting solution is a starburst template at  $z = 1.19_{-0.14}^{+0.33}$ . The northern 1.4 GHz object is not associated with any visible-light detection, although it is prominent in the IRAC and MIPS images. Those images also show two more sources: an easterly object whose SED suggests it is a star or a low redshift elliptical galaxy, and well to the west, the QSO RDS 054A at  $z = 2.416$  (Schmidt et al. 1998), which is not expected to make a strong contribution to the  $350\ \mu\text{m}$  emission.
- LH 350.2: the 1.4 GHz image shows three sources within the beam. However, the two outermost objects are well-resolved in the visible imaging, suggesting that they are likely to be relatively nearby. Photo- $z$  fitting puts both at  $z \sim 0.4$ , and SED template fitting puts a contribution to the  $350\ \mu\text{m}$  emission of  $<20\%$  (assuming a dust temperature,  $T_d > 30\ \text{K}$ ). Therefore, the very red middle object is likely to be the predominant source of the  $350\ \mu\text{m}$  emission with a best-fitting photo- $z$  of  $1.21_{-0.20}^{+0.13}$ .
- LH 350.3: there is a strong  $24\ \mu\text{m}$  and weak 1.4 GHz source within  $6''$  of the  $350\ \mu\text{m}$  position. The *B* through  $4.5\ \mu\text{m}$  images suggest that the mid-IR flux is a combination of two sources with the radio position lining up on the redder, western object. Best-fitting photometric redshifts are  $z = 2.47_{-0.97}^{+0.51}$  and  $z = 0.56_{-0.39}^{+0.28}$  for the western and eastern objects respectively. There remains the possibility of a merging system because the secondary solution for the eastern source is  $z = 2.60_{-0.33}^{+0.32}$ . Based on the radio identification, the western object is taken as the main source of the submillimeter emission.

### 3. Constraints on the photometric redshift and thermal emission

The multiwavelength photometry in Table 2 was used to derive photometric redshifts and thermal emission parameters. Following the same approach as Khan et al. (2005), the STARDUST2 template fit was used (Chanical 2009) to simultaneously obtain the photometric redshift  $z_{\text{phot}}$ , dust temperature  $T_d$ , and the 8–1000  $\mu\text{m}$  IR luminosity  $L_{\text{IR}}$ . Templates were based on local starbursts, and  $\chi^2$  was minimised through a Levenberg-Marquardt technique. For SSG 1, the redshift obtained for the IRS spectrum in Figure 1 was used in the fit, but  $z_{\text{spec}} = 1.05$  agrees well with the  $z_{\text{phot}} = 1.03$  from the template fitting. The best-fit parameters are given in Table 3, and the best-fitting templates shown in Figure 3.

For SSG 1, SSG 2, and LH 350.3 the 350  $\mu\text{m}$  flux density is well fit by the template, but in the cases of LH 350.2 and 3, the quality of the fit at 350  $\mu\text{m}$  is clearly affected by the longer submillimeter data, which constrain the slope on the Rayleigh-Jeans side of the spectrum. Additionally, the 24  $\mu\text{m}$  flux density is useful in determining which side of the peak the 350  $\mu\text{m}$  datapoint lies. Usually the mid-IR is not used to constrain the restframe far-IR continuum emission because specific dust grains and AGN can have a major effect on mid-IR flux densities. Usage of the MIPS band was checked for a sample of SMGs (from Coppin et al. 2008) by comparing template fits using measurements at 350  $\mu\text{m}$ , 850  $\mu\text{m}$ , and radio with measurements at 24  $\mu\text{m}$ , 350  $\mu\text{m}$ , and radio plus long-submillimeter limits. The two approaches agree within the STARDUST2 uncertainties. This indicates our thermal parameters are not noticeably biased by the inclusion of the mid-IR data. (See Chanical 2009 for more details.)

For LH 350.3, the lack of a defining 1.6  $\mu\text{m}$  rest-frame stellar continuum feature makes a significant AGN contribution plausible, although the relatively low radio flux density would argue against this. Because of the absence of AGN templates in STARDUST2, the LH 350.3 data were also fit using another routine with a mixture of AGN and starburst templates (Negrello et al. 2009). In this template fit, the favoured solution is a starburst at  $z_{\text{phot}} = 3.8$  (but without including the radio flux density). Therefore we consider LH 350.3 to be, like the rest of this sample, predominantly star-forming. Given the photometric redshift estimates from hyper-z, STARDUST2, and Negrello et al. (2009), it is possible that LH 350.3 is the most distant galaxy so far discovered at short-submillimeter wavelengths.

#### 3.1. Energy source diagnostics

As can be seen in Figure 3, all five sources are well fit in the mid-IR by templates that include features associated with star formation, i.e., a rest-frame 1.6  $\mu\text{m}$  stellar continuum

bump and apparent PAH emission. For SSG 1, the presence of PAH is confirmed by the mid-IR spectrum, shown in Figure 1. An emission line from [Ne II] is likely present though blended with possible PAH emission at  $12.7 \mu\text{m}$ . The dust continuum is relatively flat until (rest wavelength)  $\sim 15.5 \mu\text{m}$ . Although the  $9.7 \mu\text{m}$  silicate absorption is relatively weak, it is within the range seen in local IR-luminous galaxies. Table 4 gives the emission feature fluxes, and a standard template (IRAS 22491–1808, an IR-luminous galaxy with moderately strong PAH emission) was used to obtain an overall best-fitting redshift from the spectral features of  $1.05 \pm 0.01$ .

The values of  $L_{\text{PAH}}$  for the  $7.7$  and  $11.3 \mu\text{m}$  rest-frame emission ( $6.8$  and  $2.0 \times 10^9 L_{\odot}$ ) are consistent with the  $L_{\text{PAH}}$  vs  $L_{\text{IR}}$  distribution of Pope et al. (2008) for a sample of  $850 \mu\text{m}$ -selected SMGs. (This comparison used the integrated line flux densities with the  $L_{\text{IR}}$  given in Table 3). The  $7.7 \mu\text{m}$  PAH luminosity also provides an estimate of the star formation rate (SFR) of  $340 M_{\odot} \text{yr}^{-1}$  following the relation given by Weedman & Houck (2008). Given the strong star-forming features in the mid-IR spectrum, this compares favorably with the SFR derived from  $L_{\text{IR}}$  of  $136 M_{\odot} \text{yr}^{-1}$  following the relation given by Kennicutt (1998).

#### 4. Discussion

The different survey depths make it complicated to produce fair statistics for number counts. The Lockman Hole surveys (Laurent et al. 2006; Coppin et al. 2008) were targeted at known sources, and sensitivity for serendipitous sources varied with distance from the target source. Even the blank field survey in Boötes had sensitivity varying with location. (See Fig. 3 of Khan et al. 2007.) However, simply considering the flux densities of the five detections and the total survey area ( $15.1 \text{ arcmin}^2$ )<sup>1</sup>, we estimate resolving  $\sim 20\%$  of the  $350 \mu\text{m}$  contribution to the cosmic infrared background (CIB; Fixsen et al. 1998) at  $S > 17 \text{ mJy}$ . This fraction is reasonable given that the bulk of the background will be generated by galaxies near the break in the differential counts. It is also consistent with the  $30\%$  estimate at  $S > 13 \text{ mJy}$  from the source counts of Khan et al. (2007).

A lower limit on the star formation rate density (SFRD) can be found using the thermal parameters in Table 3 and the comoving volume in  $1 < z < 3$ . The conversion from far-IR luminosity to SFR is given by Kennicutt (1998). The result for this epoch is  $0.017 M_{\odot} \text{yr}^{-1} \text{Mpc}^{-3}$ , much lower than the values presented by Hopkins & Beacom (2006). This implies the bulk of the  $350 \mu\text{m}$  contribution to the star formation rate density is from less

---

<sup>1</sup>5.8 arcmin<sup>2</sup> for the Boötes observations; for LH 350.1 and 2 (Laurent et al. 2006) the map area is assumed to be that of the arguably similar SHADES observation of LH 350.3 of  $3.1 \text{ arcmin}^2$ ; Coppin et al. 2008)



luminous infrared galaxies and normal galaxies, consistent with observations of IR-luminous galaxies in different bands (e.g., Le Floch et al. 2005) and the predictions from source count models (e.g., Pearson & Khan 2009).

Our  $350\ \mu\text{m}$ -selected galaxies can be compared with sources selected at longer submillimeter wavelengths. Suitable samples that include  $350$  and  $24\ \mu\text{m}$  photometry come from Coppin et al. (2008), Laurent et al. (2006), and Kovács et al. (2006). The photometric redshifts and thermal parameters for these SMGs were again found using STARDUST2. Where there is no spectroscopic redshift, the photo- $z$  was obtained from optical and mid-IR magnitudes given by Dye et al. (2008) and Clements et al. (2008). Following the  $L_{\text{IR}}-T_d$  distribution by Blain et al. (2004), there appear to be two trends separating the predominantly local *IRAS* galaxies from the higher redshift SMGs. (See Fig. 4.) Compared with those selected at  $850$  and  $1100\ \mu\text{m}$ , the  $350\ \mu\text{m}$ -selected sources have similar dust temperatures and give no indication of temperature bias according to selection wavelength. Deeper  $800$ – $1000\ \mu\text{m}$  imaging (e.g., with ALMA — Wootten & Thompson 2009) of the  $350\ \mu\text{m}$ -selected population would provide a more direct comparison of any selection biases.

Mid-IR surveys to probe the  $1 < z < 3$  galaxy population have the advantage of better angular resolution, aiding counterpart identification (and hence more reliable redshift estimation), but a significant disadvantage is that without further far-IR observations, constraints on the rest-frame far-IR thermal emission must be indirectly inferred. The  $350:24$  flux density–redshift distribution for the SHARC II  $350\ \mu\text{m}$ -selected SMGs compared with the  $850$  and  $1100\ \mu\text{m}$ -selected SMGs is shown in Figure 5 alongside colors from various templates from Efstathiou et al. (2000). The overall distribution suggests that all samples are drawn from the same IR-luminous galaxy population, and the good agreement with the templates suggests these are predominantly luminous and ultraluminous infrared galaxies.<sup>2</sup>

Studies of infrared galaxies are often limited by unavailability of data at wavelengths longer than  $24\ \mu\text{m}$ . In such cases, the IR luminosity can be estimated using only the  $24\ \mu\text{m}$  flux density and various SED templates (Chary & Elbaz 2001) combined with an estimated redshift. For the SMG samples, the thermal emission estimates found this way compare surprisingly well with those from STARDUST2 for  $z \lesssim 1$  as shown in Figure 6. For these galaxies, the dominant errors on both luminosity predictors will arise from the photo- $z$  fitting; these errors are highly non-Gaussian and non-trivial to determine. To some extent, the agreement in Figure 6 can be attributed to small number statistics and selection. The overall variation in the ratio over a wider redshift range could also imply a heterogeneous SMG population. This would be consistent with the color in Figure 5 but with a varying degree

---

<sup>2</sup> $10^{11} < L_{\text{IR}} < 10^{12} L_{\odot}$  and  $L_{\text{IR}} > 10^{12} L_{\odot}$  respectively.

of AGN contribution. Another condition on this sample is the requirement of bright optical, mid-IR, and most importantly radio identifications; at high redshift, an AGN will boost the radio flux density and the emission in other bands (notably in the mid-IR), allowing this type of analysis to be performed. However none of the sources in the sample appears to be strongly affected by an AGN. At higher redshifts multiwavelength analysis becomes much more difficult. Some of the higher- $z$  850/1100  $\mu\text{m}$  galaxies could simply have incorrectly identified 24  $\mu\text{m}$  counterparts (see, e.g., Younger et al. 2007).

The restframe 12  $\mu\text{m}$  flux density has been suggested to be a “pivot point” for SEDs (Spinoglio et al. 1995; see also Elbaz et al. 2002), giving a fixed  $L_{12}/L_{\text{FIR}}$  for both starbursts and AGN. This correlation was determined from local *IRAS* sources, but at  $z \sim 1$ , the rest frame 12  $\mu\text{m}$  is shifted into the 24  $\mu\text{m}$  band, and thus the relation at this redshift can be examined directly by our sample. We expect this relation to hold if the populations are similar. An observed difference in the populations is that distant mid-IR sources show stronger dust grain emission features around 12  $\mu\text{m}$  compared to the local IR-luminous galaxy population. This difference could be due to differing AGN fractions (Wu et al. 2009).

Figure 7 shows the ratio of far-IR luminosity to observed *Spitzer*/MIPS 24  $\mu\text{m}$  monochromatic luminosity as a function of redshift. The ratio flattens out at  $z \sim 1$  as the rest frame 12  $\mu\text{m}$  emission is shifted into the MIPS 24  $\mu\text{m}$  band, but the dispersion increases at higher redshift. This suggests that the local empirical far-IR/12  $\mu\text{m}$  relation could apply to earlier epochs where the galaxy is undergoing rapid evolution, making rest-frame 12  $\mu\text{m}$  flux densities a better tracer of IR luminosity (Spinoglio et al. 1995) than other mid-IR emission features, e.g., 7.7  $\mu\text{m}$  PAH selected at  $z \sim 2$ . At  $z \sim 1.4$  the silicate absorption feature is redshifted into the MIPS 24  $\mu\text{m}$  band and affects the flux density measurement. This effect is emphasized in Figure 5, where an excess in the 350/24  $\mu\text{m}$  colours is evident in the model SEDs, and galaxies in the redshift range where the silicate feature would cause a deficit in the 24  $\mu\text{m}$  flux ( $1.3 < z < 1.6$ ) are notably absent from Figure 7.

Various studies have suggested that the far-IR luminosity can be deduced solely from mid-IR observations of galaxies. Bavouzet et al. (2008) have shown that the far-IR luminosity of dusty galaxies observed with *Spitzer* correlate closely with the corresponding 8 and 24  $\mu\text{m}$  mid-IR luminosities. These studies were limited to redshifts  $z \lesssim 1$  by the necessity to use *Spitzer* bands at 70 and 160  $\mu\text{m}$  to calculate the far-IR luminosity. The mid-IR to far-IR luminosity relation was tentatively extended to higher redshifts ( $z \sim 2$ ) by stacking the far-infrared fluxes in the long wavelength *Spitzer* bands, and these stacked results were used by Caputi et al. (2007) to calculate the bolometric luminosity function at  $z \approx 2$ . In contrast, our submillimeter observations directly access the high redshift Universe without the need for stacking images to obtain far-infrared fluxes. From Figure 7 we observe a tight

correlation between the far and mid-IR flux densities in our sample between  $1 < z < 2$ , but there is a large dispersion in the infrared colours at  $z > 2$ . For  $z > 2$ , the  $24\ \mu\text{m}$  band is sampling rest wavelengths shorter than  $8\ \mu\text{m}$ , and the far-IR luminosity cannot be accurately predicted from such observations. In order to confirm the mid-IR/far-IR relation for  $1 < z < 2$  and to test the relation to higher redshifts, large samples of SMGs will be required. Such samples will be available following the large surveys planned with Herschel SPIRE (at  $250$ ,  $350$ , and  $500\ \mu\text{m}$ ; Griffin et al. 2008) .

## 5. Conclusion

The discovery of the first  $350\ \mu\text{m}$ -selected galaxies using SHARC II offers a different insight into IR-luminous galaxies than those selected in either the mid-IR or in longer submillimeter bands. The present sample comprises IR-luminous galaxies at  $1 < z < 3$  and resolves  $\sim 20\%$  of the  $350\ \mu\text{m}$  background at  $S > 17\ \text{mJy}$ . The implied lower limit on the star formation rate density suggests that the bulk of the  $350\ \mu\text{m}$  contribution is from galaxies of lower IR luminosity than the ones detected at present flux densities.

The combination of  $350\ \mu\text{m}$  and mid-IR flux densities allows us to examine the relation of the mid and far-IR emission in dusty galaxies at high-redshift. There is surprisingly good agreement at  $z < 2$ , with the flattening of the  $\text{IR}:24\ \mu\text{m}/(1+z)$  luminosity ratio at  $z \sim 1$  evidence for the local empirical relation of rest frame  $12\ \mu\text{m}$  IR luminosity tracing IR luminosity applying to distant IR-luminous galaxies. The wider dispersion at  $z > 2$  suggests a limit to which the mid-IR can be used as a proxy for far-IR emission. We also find, by comparing our  $350\ \mu\text{m}$ -selected sample to samples chosen at  $850\ \mu\text{m}$  and millimeter wavelengths, no evidence for a cold color temperature bias in SMGs. These results will be further tested through surveys with *Herschel*-SPIRE, which will detect SMGs in unprecedented numbers.

The present  $350\ \mu\text{m}$ -selected sample, with  $15 < S_{350} < 40\ \text{mJy}$ , is near the SPIRE  $350\ \mu\text{m}$  blank-field detection limit (e.g., Pearson & Khan 2009; Franceschini et al. 2009) and also the detection limits of current longer-wavelength submillimeter instruments. Counterpart identification is difficult even with the available angular resolution and will be far more difficult for space-based surveys with smaller telescopes. The achievable sensitivity and resolution of ground-based detectors will therefore provide a necessary complement to the space-based surveys, especially in characterising the nature of the faint SMG population. Whether the first  $350\ \mu\text{m}$ -selected galaxies are typical of the population will be probed through the combination of surveys with SPIRE and future surveys from the ground (e.g., SCUBA 2– $450\ \mu\text{m}$ ; Holland et al. 2006).

We thank Tom Phillips and the CSO for observing time and assistance during our runs and Darren Dowell, Colin Borys, Attila Kovacs, Rick Arendt, Dave Chuss, and Bob Silverberg for providing observing and data reduction support. We thank Glenn Laurent and Kristen Coppin for advice on their 350  $\mu\text{m}$  Lockman Hole follow-up surveys, Mark Brodwin and Yen-Ting Lin for assistance in compiling the Boötes optical and near-IR photometry, and Rob Ivison for providing the radio maps for the Lockman Hole sources.

The Caltech Submillimeter Observatory is supported by NSF contract AST-0229008. This work is based in part on observations made with the Spitzer Space Telescope, which is operated by the Jet Propulsion Laboratory, California Institute of Technology under a contract with NASA. This work is based in part on data collected at Subaru Telescope, which is operated by the National Astronomical Observatory of Japan. The Subaru data are those used by Dye et al. (2008). This research has made use of the NASA/IPAC Extragalactic Database (NED), which is operated by the Jet Propulsion Laboratory, California Institute of Technology, under contract with the National Aeronautics and Space Administration. This research has made use of the SIMBAD database, operated at CDS, Strasbourg, France. This research draws upon data provided by Buell Jannuzi & Arjun Dey and by Richard Elston & Anthony Gonzalez (Elston et al. 2006) as distributed by the NOAO Science Archive. NOAO is operated by the Association of Universities for Research in Astronomy (AURA), Inc. under a cooperative agreement with the National Science Foundation. The UKIDSS project is defined by Lawrence et al. (2007). UKIDSS uses the UKIRT Wide Field Camera (WFCAM; Casali et al. 2007). We used data from the fourth data release (DR4).

S.A.K. is partially supported through FONDECYT Proyecto 1070992 and ALMA-Conicyt. Support for E.L.F.’s work was provided by NASA through the Spitzer Space Telescope Fellowship Program.

Facilities: CSO, Spitzer, UKIRT, Subaru, VLA

## REFERENCES

- Aussel, H., Elbaz, D., & Cesarsky, C. J. 1999, *Ap&SS*, 266, 307
- Barger, A. J., et al., 1998, *Nature*, 394, 248
- Bavouzet, N., Dole, H., Le Floc’h, E., Caputi, K. I., Lagache, G., Kochanek, C.S., *A&A*, 479, 83
- Bertoldi, F., et al. 2000, *A&A*, 360, 92
- Biggs, A.D., & Ivison, R.J., 2006, *MNRAS*, 371, 963

- Blain, A. W., Chapman, S. C., Smail, I., Ivison, R., 2004, ApJ, 611, 52
- Bolzonella, M., Miralles, J.-M., & Pell’o, R., 2000, A&A, 363, 476
- Caputi, K.I., et al., 2007, ApJ, 660, 116
- Casali, M., et al., 2007, A&A, 467, 777
- Chanial, P.F., 2009, in preparation
- Chapman, S. C., Blain, A. W., Smail, I., Ivison, R. J., 2005, ApJ, 622, 772
- Chary, R., & Elbaz, D., 2001, ApJ, 556, 562
- Chary R. et al., 2004, ApJS, 154, 80
- Clements, D.L., et al., 2009, in preparation
- Clements, D.L., et al., 2008, MNRAS, 387, 247
- Coppin, K., et al., 2008, MNRAS, 384, 1597
- Dowell C.D., et al., 2003, SPIE, 4855, 73
- Dunne, L., et al., 2000, MNRAS, 315, 115
- Dye, S., et al., MNRAS, 386, 1107
- Eales, S., et al., 1999, ApJ, 515, 518
- Eisenhardt, P.R., et al., 2004, ApJS, 154, 48
- Elbaz, D., Cesarsky, C.J., Chanial P., Aussel H., Franceschini, A., Fadda, D., Chary, R.R.,  
2002,AA, 384, 848
- Elbaz, D. 2005, Space Science Reviews, 119, 93
- Elston, R. J., et al. 2006, ApJ, 639, 816
- Efstathiou A., Rowan-Robinson M., Siebenmorgen R., 2000, MNRAS, 313, 734
- Fazio, G.G., et al., 2004, ApJS, 154, 10
- Fixsen, D.J., et al., 1998, ApJ, 508, 123
- Fox M. et al., 2002, MNRAS, 331, 839

- Franceschini, A., Rodighiero, G., Vaccari, M., Marchetti, L., & Mainetti, G. 2009, *A&A*, submitted (arXiv:0906.4264)
- Galliano, F., et al., 2008, *ApJ*, 679, 310
- Gordon, K.D., et al., 2005, *PASP*, 117, 503
- Griffin, M., et al., 2008, *SPIE*, 7010, 4
- Higdon, S.J.U., et al., 2004, *PASP*, 116, 975
- Holland, W. S., et al., 2006, *SPIE*, 6275, 45
- Holland, W. S., et al., 1999, *MNRAS*, 303, 659
- Houck, J.R., et al., 2004, *ApJS*, 154, 18
- Hauser, M.G., & Dwek, E., 2001, *ARA&A*, 39, 249
- Hopkins, A.M., Beacom, J.F., 2006, *ApJ*, 651, 1
- Joseph R.D., Wright G.S., 1985, *MNRAS*, 214, 87
- Kessler, M.F., et al., 1996, *A&A*, 315, 27
- Khan, S.A. et al. 2005, *ApJ* 631, L9
- Khan, S.A., 2006, PhD Thesis, University of London
- Khan, S. A., et al. 2007, *ApJ*, 665, 973
- Kovács, A., et al., 2006, *ApJ*, 650, 592
- Kennicutt, R.C., Jr, 1998, *ApJ*, 498, 541
- Laurent, G. T., et al. 2006, *ApJ*, 643, 38
- Laurent, G. T., et al. 2005, *ApJ*, 623, 742
- Lawrence, A., et al., 2007, *MNRAS*, 379, 1599
- Le Floc'h, E., et al. 2004, *ApJS*, 154, 170
- Le Floc'h, E., et al., 2005, *ApJ*, 632, 169
- Lonsdale, C., et al. 2004, *ApJS*, 154, 54

- Matsuhara, H., et al., 2006, PASJ, 58, 673
- Moseley S.H., et al., 2004, NIMPA, 520, 417
- Murakami, H., et al. 2007, PASJ, 59, 369
- Negrello, M., et al. 2009, MNRAS, 394, 375
- Pearson, C.P. & Khan, S.A., 2009, Letters to MNRAS, in press
- Pope, A., et al., 2008, ApJ, 675, 1171
- Puget, J. L., et al. 1999, A&A, 345, 29
- Rieke, G.H., et al., 2004, ApJS, 154, 25
- Rowan-Robinson, M., et al. 1997, MNRAS, 289, 490
- Schmidt, M., et al., 1998, A&A, 329, 495
- Schuster, M.T., Marengo, M., & Patten, B.M., 2006, SPIE
- Serabyn, E., Weisstein, E. W., Lis, D. C., & Pardo, J. R. 1998, Appl. Opt., 37, 2185
- Smail I., Ivison R.J., Blain A.W., 1997, ApJ, 490, L5
- Smail I., Ivison R.J., Blain A.W., Kneib J.-P., 2002, MNRAS, 331, 495
- Smith, J.D.T., et al., 2007, ApJ, 656, 770
- Soifer B.T., Neugebauer G., Houck J.R., 1987, ARA&A, 25, 187
- Soifer B.T., et al., 1984, ApJ, 278L, 71
- Spinoglio, L., et al., 1995, ApJ, 453, 616
- Weedman, D.W., & Houck, J.R., 2008, ApJ, 686, 127
- Werner, M.W., et al., 2004, ApJS, 154, 1
- Wootten, A., & Thompson, A. R. 2009, Proc. IEEE, 97, 1463
- Wu, Y., Charmandaris, V., Huang, J., Spinoglio, L., & Tommasin, S. 2009, ApJ, 701, 658
- Yan, L., et al. 2004, ApJS, 154, 60
- Younger, J.D., et al., 2007, ApJ, 671, 1531





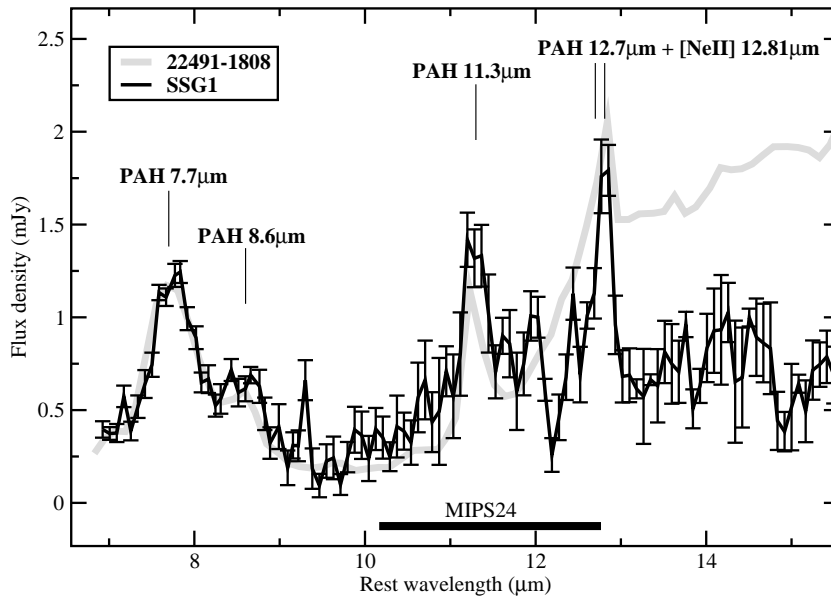


Fig. 1.— The mid-IR spectrum of SSG 1 as observed by *Spitzer* IRS, indicated by black line. One-sigma error bars are shown. Wavelengths are in the rest frame based on the derived redshift  $z = 1.05$ . The spectrum of IRAS 22491–1808, used as a template to derive the redshift, is shown in grey. Prominent dust grain emission features are also indicated. The MIPS 24  $\mu\text{m}$  passband is shown by the heavy black line below the spectrum.

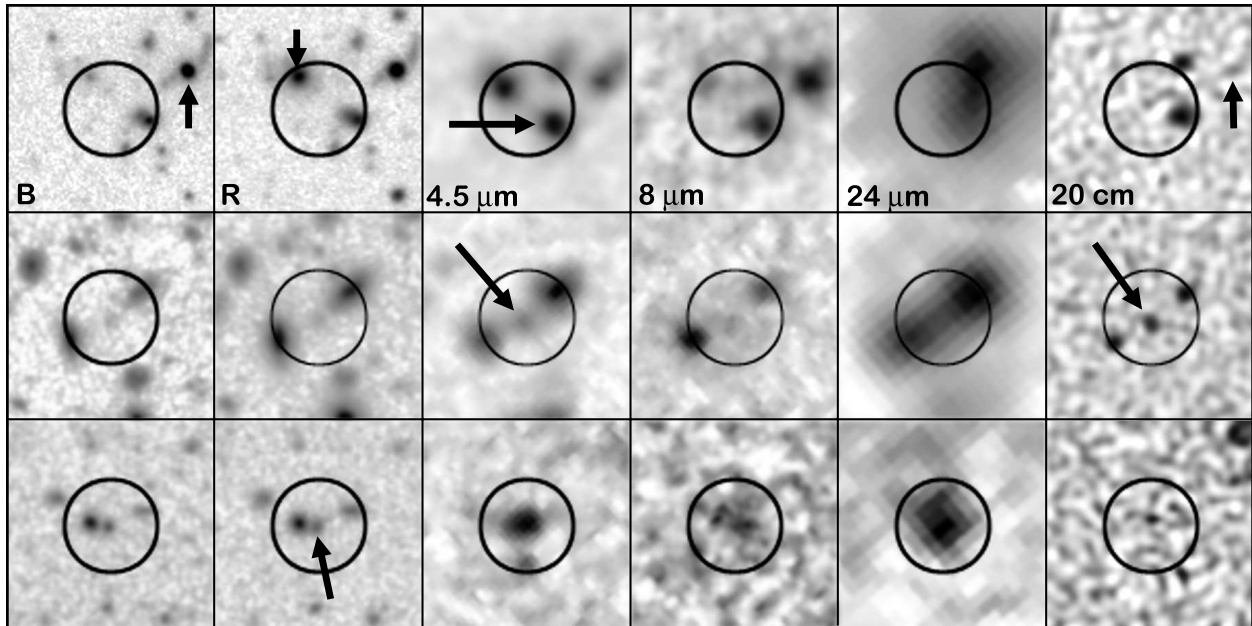


Fig. 2.— Visible, mid-IR, and radio imaging of LH 350.1 (top), LH 350.2 (middle), and LH 350.3 (bottom). Each image is  $20''$  on a side with a  $9''$  diameter circle centered on the SHARC II  $350\ \mu\text{m}$  position. North is up and east to the left. Arrows in the LH 350.1 panels indicate the unrelated QSO RDS 054A ( $B$  and  $20\ \text{cm}$  panels), a star or low-redshift E galaxy ( $R$  panel), and the proposed SMG counterpart ( $4.5\ \mu\text{m}$  panel). Arrows in the LH 350.2 and 350.3 panels indicate the proposed SMG counterparts.

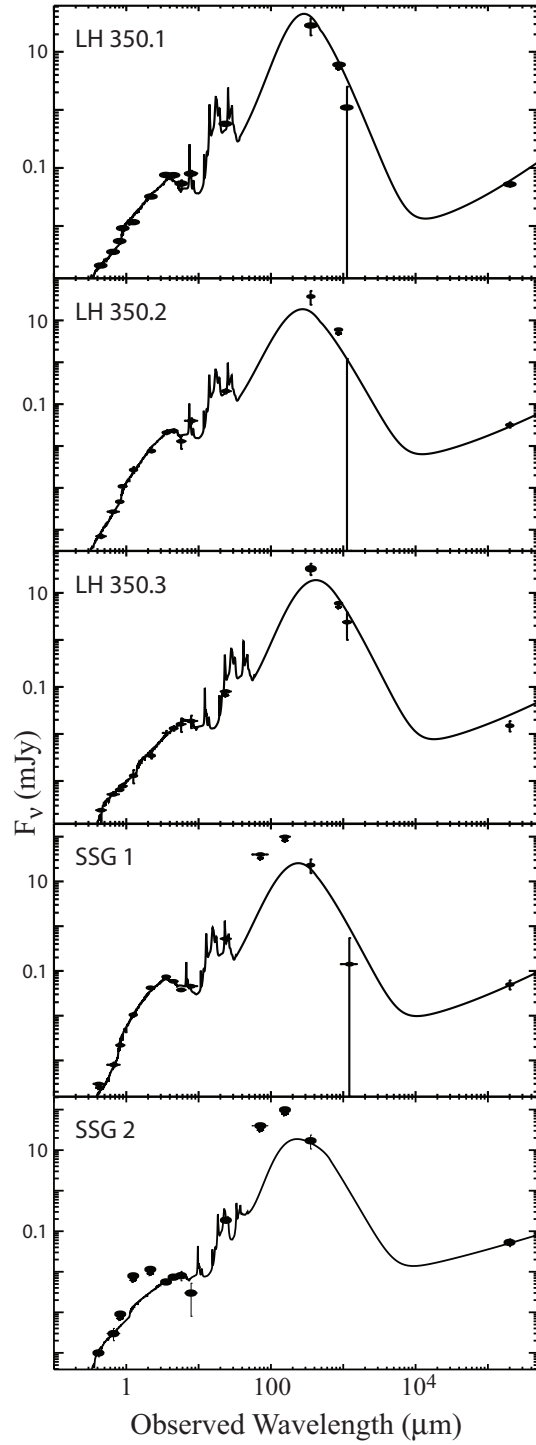


Fig. 3.— Best-fitting SED templates from STARDUST2. Wavelengths are in the observed frame.

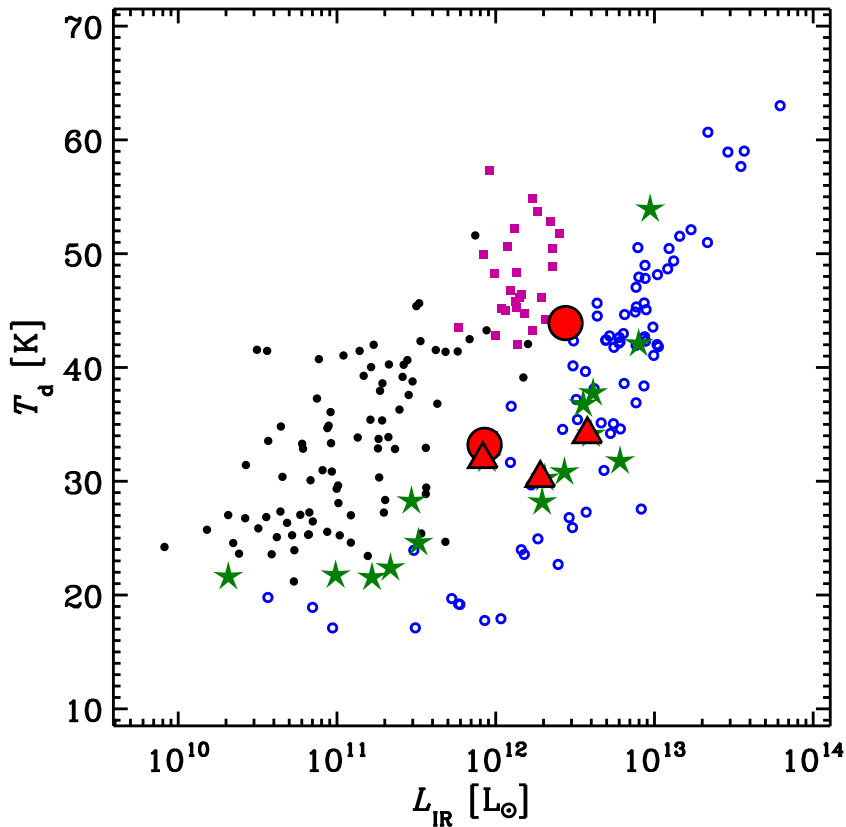


Fig. 4.— The IR luminosity-dust temperature distribution for various IR-luminous galaxy samples. For the  $350\ \mu\text{m}$ -selected galaxies, the red circles show SSG 1 and SSG 2, and triangles show LH 350.1, 350.2, and 350.3. Green stars represent the  $850$  and  $1100\ \mu\text{m}$ -selected SMGs for which there is  $350\ \mu\text{m}$  follow-up photometry. This is compared with  $850\ \mu\text{m}$ -selected SMGs from Chapman et al. (2005) (open blue circles) and *IRAS* galaxies from Dunne et al. (2000) (filled black squares) and Clements et al. (2009) (purple squares).

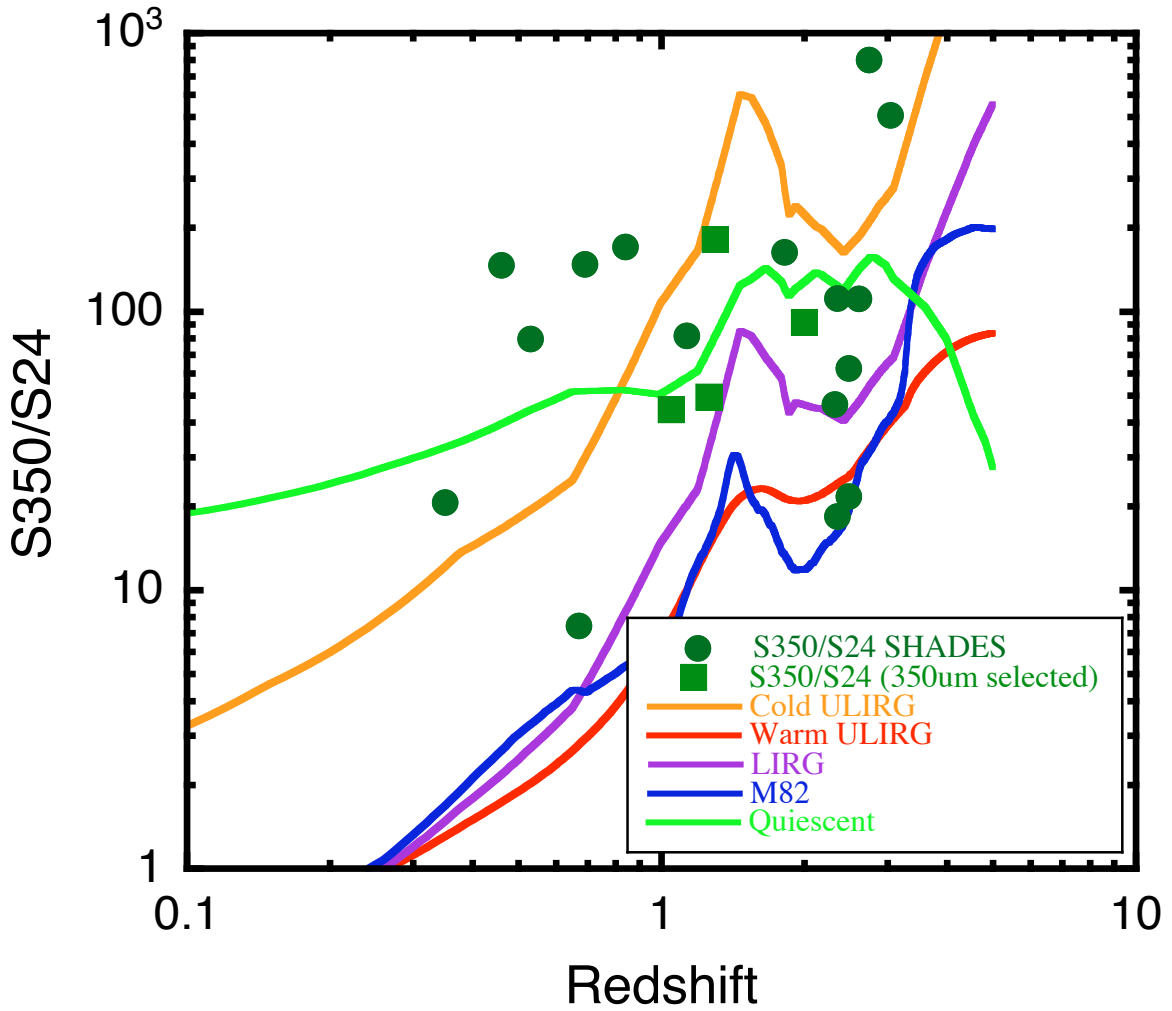


Fig. 5.— The  $350\ \mu\text{m}:24\ \mu\text{m}$  flux density ratio as a function of redshift for various SMG samples as indicated in the legend. Lines show the same ratio for local SED templates from Efstathiou et al. (2000).

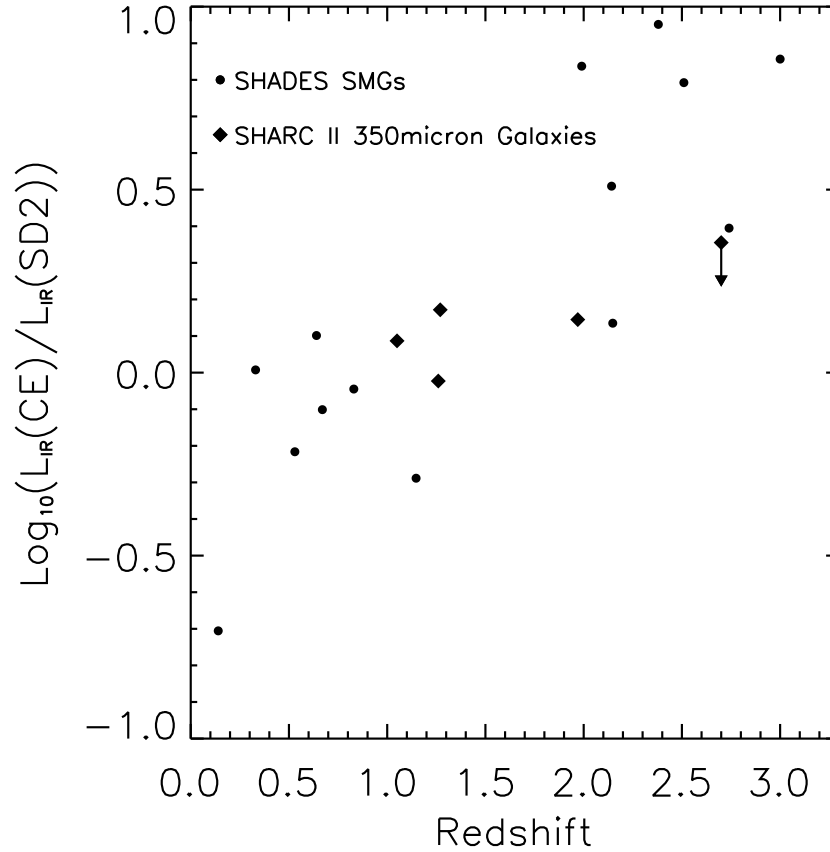


Fig. 6.— The ratio of best-fitting IR (8–1000  $\mu\text{m}$ ) luminosities obtained from the CE and STARDUST2 fitting, as a function of redshift. The diamonds denote the 350  $\mu\text{m}$ -selected galaxies, and filled circles denote the 850 and 1100  $\mu\text{m}$ -selected galaxies. The diamond with arrow denotes an upper limit. Sources with redshifts beyond the useable range for the CE model ( $\sim 3$ ) are excluded from consideration.

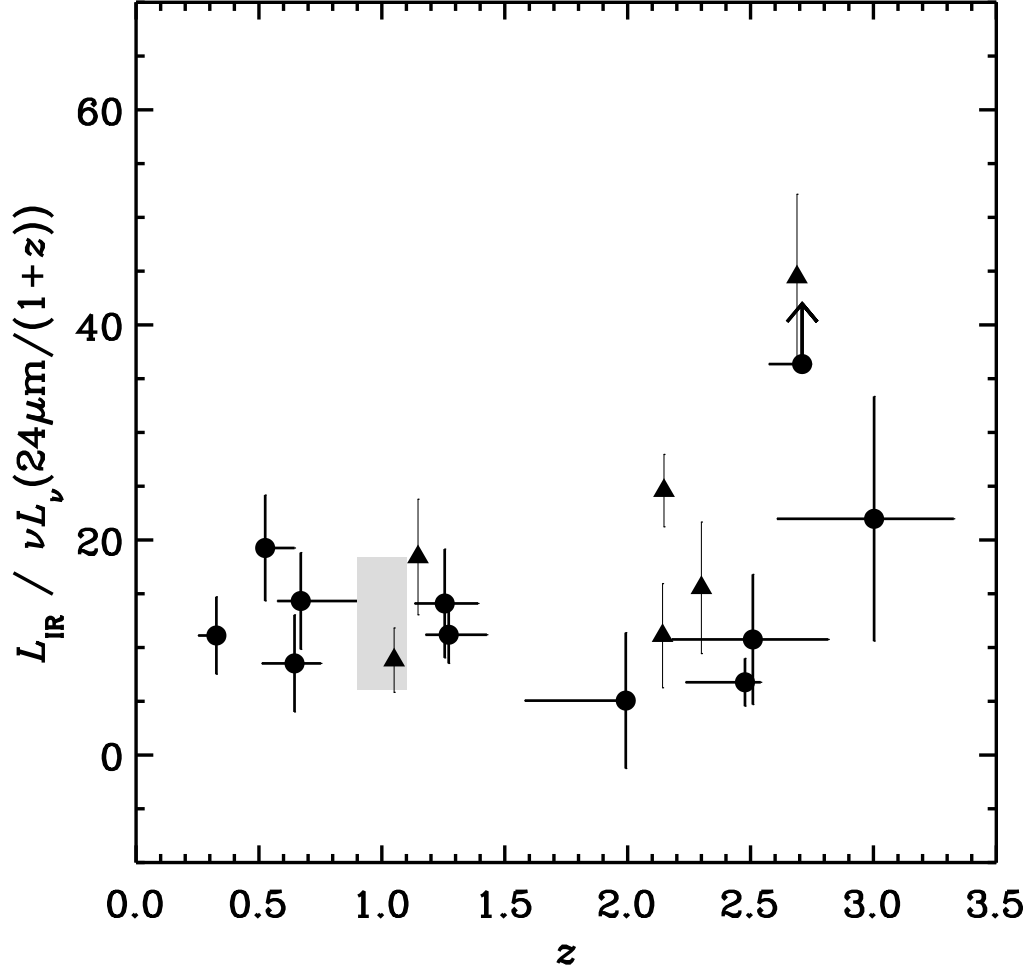


Fig. 7.— Ratio of far-IR luminosity to monochromatic luminosity at observed wavelength  $24\ \mu\text{m}$  as a function of redshift. Data are shown for the 350, 850, and  $1100\ \mu\text{m}$ -selected SMGs. Numerator of the ratio is the rest frame far-IR ( $8\text{--}1000\ \mu\text{m}$ ) luminosity derived from the STARDUST2 template fitting. The denominator is the rest frame luminosity for the  $24\ \mu\text{m}$  observation, i.e., monochromatic luminosity  $\nu L_\nu$  at rest frame wavelength  $24\ \mu\text{m}/(1+z)$ . At  $z \approx 1$ , observed  $24\ \mu\text{m}$  corresponds to rest  $12\ \mu\text{m}$ , which as Spinoglio et al. (1995) suggested gives a good measure of total luminosity. The shaded region on the plot shows the Spinoglio et al. data for local luminous infrared galaxies as they would appear at  $z = 1$ . Filled triangles denote sources with spectroscopic redshift, while filled circles denote sources with photometric redshifts from the STARDUST2 template fit.

Table 1: The first five 350  $\mu\text{m}$ -selected galaxies

Name [IAU] (nickname)	Position [VLA] (J2000)	
Other names	Position [350 $\mu\text{m}$ ] (J2000)	
SMM J143206.65+341613.4 (SSG 1)	14 32 06.58	+34 16 11.9
	14 32 06.65	+34 16 13.4
SMM J143206.11+341648.4 (SSG 2)	14 32 06.04	+34 16 46.7
	14 32 06.11	+34 16 48.4
SMM J105308.3+571501 (LH 350.1)	10 53 07.89	+57 15 00.3
SHARC II Source 3	10 53 08.3	+57 15 01
SMM J105232.3+572448 (LH 350.2)	10 53 32.26	+57 24 47.4
SHARC II Source 4	10 52 32.3	+57 24 48
SMM J105243.2+572309 (LH 350.3)	10 52 43.17	+57 23 09.7
LOCK 350.1	10 52 43.2	+57 23 09

VLA positions are for identified VLA counterparts. The 350  $\mu\text{m}$  position is used for the IAU name.



Table 2: Photometry for counterparts of 350  $\mu\text{m}$ -selected galaxies

$\lambda_{obs}$	SSG 1	SSG 2	LH 350.1	LH 350.2	LH 350.3
$B$ [ $\mu\text{Jy}$ ]	<0.3	0.1 $\pm$ 0.02	2.1 $\pm$ 0.020	0.07 $\pm$ 0.007	0.24 $\pm$ 0.009
$R$	0.8 $\pm$ 0.1	0.3 $\pm$ 0.1	3.6 $\pm$ 0.033	0.27 $\pm$ 0.013	0.52 $\pm$ 0.014
$I$	2.2 $\pm$ 0.1	< 0.9	5.5 $\pm$ 0.051	0.47 $\pm$ 0.017	0.65 $\pm$ 0.018
$z$	...	...	9.2 $\pm$ 0.085	1.09 $\pm$ 0.040	0.78 $\pm$ 0.036
$J$	10.5 $\pm$ 1.1	< 7.9	11.7 $\pm$ 0.65	2.7 $\pm$ 0.45	1.3 $\pm$ 0.41
$K$	42.0 $\pm$ 1.4	< 11.5	32.2 $\pm$ 0.89	7.6 $\pm$ 0.56	<1.5
3.6 $\mu\text{m}$	73.8 $\pm$ 0.3	5.6 $\pm$ 0.3	75.5 $\pm$ 7.0	21.1 $\pm$ 2.0	10.5 $\pm$ 1.1
4.5 $\mu\text{m}$	58.5 $\pm$ 0.5	7.4 $\pm$ 0.5	74.8 $\pm$ 6.9	23.0 $\pm$ 2.2	13.2 $\pm$ 1.5
5.8 $\mu\text{m}$	37.7 $\pm$ 2.1	8.1 $\pm$ 2.1	54.2 $\pm$ 7.0	13.0 $\pm$ 4.5	16.2 $\pm$ 5.2
8.0 $\mu\text{m}$	45.8 $\pm$ 2.2	3.0 $\pm$ 2.2	80.7 $\pm$ 8.6	40.1 $\pm$ 6.0	18.9 $\pm$ 5.6
24 $\mu\text{m}$	523.8 $\pm$ 58.7	187.2 $\pm$ 29.4	576 $\pm$ 13 <sup>a</sup>	204 $\pm$ 24 <sup>a</sup>	<80.2 <sup>b</sup>
70 $\mu\text{m}$ [mJy]	< 40	< 40	...	...	...
160 $\mu\text{m}$	< 100	< 100	...	...	...
350 $\mu\text{m}$	23.2 $\pm$ 7.9	17.1 $\pm$ 6.4	28.4 $\pm$ 9.2	37.0 $\pm$ 13.4	32.8 $\pm$ 8.9
850 $\mu\text{m}$	...	...	<6	<6	<6
1100 $\mu\text{m}$	...	...	1.1 $\pm$ 1.4	-0.2 $\pm$ 1.4	2.4 $\pm$ 1.4
1200 $\mu\text{m}$	0.142 $\pm$ 0.4	...	...	...	...
20 cm [ $\mu\text{Jy}$ ]	49.8 $\pm$ 11.4	53.1 $\pm$ 11.4	52.5 $\pm$ 5.2	32.0 $\pm$ 4.6	15.8 $\pm$ 4.8

For non-detections, the flux density at the radio position is used. Upper limits are  $3\sigma$ .

These data are used in the STARDUST2 SED template fitting.

<sup>a</sup>Flux density is deblended using [3.6]  $\mu\text{m}$  positions.

<sup>b</sup>Flux density cannot be deblended, used as a limit instead.

Table 3: Best-fitting parameters from STARDUST2 template fitting.

Nickname	$\log(L_{IR}(SD2)/L_{\odot})$ [ $L_{IR}(CE)$ ] <sup>a</sup>	$T_{dust}(SD2)$	$z_{phot}(SD2)$	$S_{850}(SD2)$ <sup>b</sup> [mJy]
SSG 1	$11.9^{+0.1}_{-0.1}$ [12.0]	$33.2^{+2.3}_{-2.3}$	$1.03^{+0.16c}_{-0.14}$	$2.4 \pm 0.8$
SSG 2	$12.4^{+0.1}_{-0.1}$ [12.6]	$43.9^{+2.4}_{-9.2}$	$1.97^{+0.8}_{-0.3}$	$2.7 \pm 0.7$
LH 350.1	$12.3^{+0.10}_{-0.13}$ [12.5]	$30.3^{+1.5}_{-1.2}$	$1.27^{+0.16}_{-0.09}$	$6.7 \pm 2.7$
LH 350.2	$11.9^{+0.13}_{-0.24}$ [11.9]	$31.9^{+3.4}_{-2.8}$	$1.26^{+0.14}_{-0.12}$	$2.4 \pm 0.6$
LH 350.3	$12.6^{+0.13}_{-0.24}$ [ $<13.0$ ]	$34.1^{+2.4}_{-1.8}$	$2.71^{+0.03}_{-0.14}$	$7.6 \pm 2.0$

<sup>a</sup>The luminosity from the Chary-Elbaz template fit,  $L_{IR}(CE)$ , is obtained from the  $24\mu\text{m}$  flux density and the STARDUST2 photometric redshift  $z_{phot}(SD2)$  (or spectroscopic redshift for SSG 1).

<sup>b</sup>Predicted  $850\mu\text{m}$  flux densities from the STARDUST2 fit.

<sup>c</sup>Spectroscopic redshift for SSG 1 is  $1.05 \pm 0.01$ .

Table 4: Features in the SSG 1 spectrum

Feature	Rest wavelength [ $\mu\text{m}$ ]	Line Center [ $\mu\text{m}$ ]	Line Flux [ $10^{-22}\text{W cm}^{-2}$ ]
PAH	7.7	15.9	$14.5\pm 4.4$
PAH	8.6	17.4	$12.4\pm 1.8$
[S IV]	10.5	21.7	$1.2\pm 1.8$
PAH	11.3	23.1	$46.1\pm 5.3$
PAH	12.7	26.0	$3.0\pm 0.6$
[Ne II] <sup>a</sup>	12.8	26.9	$3.3\pm 0.4$
[Ne V]	14.3	29.7	$0.5\pm 0.3$

---

<sup>a</sup>The [Ne II] emission line could be blended with the 12.7  $\mu\text{m}$  PAH feature.